

## Article

# Surface Structuring of the CP Titanium by Ultrafast Laser Pulses

Kipkurui Ronoh <sup>1,2,3,\*</sup>, Jan Novotný <sup>4</sup>, Libor Mrňa <sup>4</sup>, Alexandr Knápek <sup>4</sup> and Dinara Sobola <sup>1,2,5,\*</sup>

<sup>1</sup> Central European Institute of Technology, Brno University of Technology, Purkyňova 123, 612 00 Brno, Czech Republic

<sup>2</sup> Department of Physics, Faculty of Electrical Engineering and Communication, Brno University of Technology, Technická 2848/8, 616 00 Brno, Czech Republic

<sup>3</sup> Department of Mechanical Engineering, Dedan Kimathi University of Technology, Private Bag, Dedan Kimathi, Nyeri 10143, Kenya

<sup>4</sup> Institute of Scientific Instruments, Czech Academy of Sciences, Královopolská 147, 612 64 Brno, Czech Republic

<sup>5</sup> Institute of Physics of Materials, Czech Academy of Sciences, Žižkova 22, 616 62 Brno, Czech Republic

\* Correspondence: kipkurui.ronoh@ceitec.vutbr.cz (K.R.); sobola@vut.cz (D.S.)

**Abstract:** Surface structuring by ultrafast lasers is a promising technique to modify surface-related properties of materials to tailor them for specific applications. In the present study, we experimentally investigated the laser structuring of commercially pure titanium (CP Ti) using ultrafast pulses to understand the role of the laser input parameters on the development of surface morphology, optical properties, surface chemistry, and wettability behaviour. The processed surfaces were characterized by a scanning electron microscope, energy-dispersive X-ray spectroscopy (EDX), Raman microscope, optical microscope, and sessile drop method. Laser-induced periodic surface structures decorated with nanodroplets were noted to be formed on the surface of the laser-structured CP Ti. The surface roughness measurements showed that the laser-structured surfaces had nanoscale roughness values. The EDX and the Raman analyses show that laser-structured surfaces of CP Ti have a thin oxide film. Different colours on different surfaces processed by different laser parameters were observed. The wettability assessment shows that CP Ti can transition from hydrophilic–hydrophobic and vice versa depending on the environmental conditions. This study shows that laser structuring can be utilized to modify CP Ti surfaces to obtain desirable surface properties that can find potential applications in different fields.

**Keywords:** CP titanium; laser structuring; surface structures; morphology; raman analysis; colourization; wettability



**Citation:** Ronoh, K.; Novotný, J.; Mrňa, L.; Knápek, A.; Sobola, D. Surface Structuring of the CP Titanium by Ultrafast Laser Pulses. *Appl. Sci.* **2024**, *14*, 3164. <https://doi.org/10.3390/app14083164>

Academic Editors: Luca Poletto and Simone Morais

Received: 10 March 2024

Revised: 26 March 2024

Accepted: 5 April 2024

Published: 9 April 2024



**Copyright:** © 2024 by the authors. Licensee MDPI, Basel, Switzerland. This article is an open access article distributed under the terms and conditions of the Creative Commons Attribution (CC BY) license (<https://creativecommons.org/licenses/by/4.0/>).

## 1. Introduction

Titanium material such as unalloyed commercially pure titanium (CP-Ti) and its alloys find applications in various fields, such as aeronautical, biomedical, chemical, petroleum, automotive, and armour applications among others, because of their unique properties [1–5]. They have excellent corrosion resistance, high specific strength, biocompatibility, and toughness among others [4,6]. Because of its usefulness, titanium and its alloys have been subjected to surface modification through various techniques to change their surface properties [7,8]. Surface structuring through laser irradiation of the titanium substrate modifies surface morphologies by creating multifunctional surfaces and changing a variety of material properties, including wetting [9–11], corrosion [4,12,13], tribological [14], antireflective [15], or bacterial adhesion qualities [16,17], among others. It is therefore important to conduct research to establish specific surface modifications of titanium and other materials for a specific application. The laser structuring technique has many advantages, such as being contactless, green, and sustainable, with no restrictions on the processing environment, the precise, automatable, processing of many types of materials, and no masks needed, among others [2,4,18,19].

It has been stated that laser structuring can find applications in the modification of optical properties of metals for applications such as permanent marking, photovoltaic cells, and decorations, among others [20–23]. Laser-induced colourization or laser colour marking in metals is one such application and this can be achieved using two main methods [20,22]. One approach uses a laser, specifically a nanosecond laser, for the generation of oxide film on the metal surface where colourization, independent of the angle of viewing, occurs through thin oxide film interference. Another approach is the use of lasers such as femtosecond (fs) or picosecond (ps) lasers to produce laser-induced periodic surface structures (LIPSSs) where the colour formation mechanism is through periodic surface diffraction grating. The colour effects produced are commonly referred to as structural colours [24] and depend on the angle of viewing [20]. Laser structuring as a method of colouring metals has been investigated previously [22,23]. It has been established that the colourization of metals depends on laser fluence, wavelength, polarization, ablation environment, and scanning velocity, among others [7,21,25–27]. Finding the approximate and optimized parameters for producing specific colours on CP Ti is therefore an exciting area of research.

It is well established that the wettability of the laser-structured surfaces depends on the topography and surface chemistry [28]. The attainment of the hydrophobicity is fundamentally due to hierarchical rough surface structures induced by laser irradiation. Some approaches, like surface coating, increase the hydrophobicity by decreasing the surface tension, and the largest achievable water contact angle on a smooth flat surface through coating is approximately 120° [23,29]. This indicates that rough surface structures amplified the attainment of (super)hydrophobicity. Tailoring of the different morphologies and topographies of the surface structures to obtain (super)hydrophobicity on CP titanium substrate depends on laser fluence, scanning velocity, laser wavelength, etc [5,17,19,30]. Many studies have been conducted using higher laser fluence and fewer studies have been done with low laser fluence. Hence, there is a need for studies involving laser processing of the CP Ti using low laser fluence in the generation of surface morphology and topography and modification of the surface chemistry and evaluate their impact on the wetting behaviour. Additionally, because the different surface structures generated such as LIPSSs have several applications, there is a need for continuous research in the same field of study to understand more the relationship between the laser processing parameters and the morphological changes.

Hence, this study aimed to do an experimental investigation to study the influence of laser processing parameters on the surface modification of the CP Ti substrate for the production of surface structures and evaluate their influence on the modification of the surface chemistry and development of colourization and wettability. The focus is on the low laser fluence to induce specific morphological changes, wetting behaviours, and alteration of the optical properties on the CP Ti. The focus is also on the wetting behaviour of the laser-structured surfaces of the CP Ti material under three conditions, i.e., before immersion, immediately after immersion, and after storage following immersion. The ps laser was chosen for the fabrication process because of its advantages of high pulse energy, high precision for micro/nanostructures, and low heat accumulation [2]. This research provides more information on how laser processing parameters can be utilised to obtain different surface morphologies and colourization which could have a broad range of uses in laser colour marking and artistic design, among others. It will also lead to more understanding of the wettability development of laser-textured metallic surfaces aimed for corrosion control, cell adhesion, antifouling behaviour, and self-cleaning surfaces, among others.

## 2. Materials and Methods

A polished commercially pure titanium (CP Ti) with 25 × 25 × 4 mm dimension was subjected to laser processing. The nominal percentage chemical compositions of the elements on the polished sample as per the Energy-dispersive X-ray spectroscopy (EDX) were Ti = 99.1%, O = 0.7%, Fe = 0.1%, Al = 0.1%, and C = 0.1%. Before laser processing, the

polished sample was ultrasonically cleaned in acetone and ethanol for 10 min each before drying using pressurized air.

The laser structuring experiments were carried out using a picosecond laser system (Perla®100, Hilase, Dolní Břežany, Czech Republic) which has a picosecond pulsed laser (Yb-YAG thin disk medium), scanning head, beam expander, and XY translational stage. The schematic set-up of the laser system has been previously published [31]. The laser source produces laser pulses with a pulse width of 1 ps, a wavelength of 1030 nm, a repetition frequency of 60 kHz, and a maximum pulse energy of 1 mJ. The focusing lens (Linos, Qioptiq, Göttingen, Germany) on the scanning head (intelliSCAN 14, Scanlab, Puchheim, Germany) ensured that the focussed spot diameter of the linearly polarised Gaussian laser beam during laser structuring experiments was  $\sim 25 \mu\text{m}$ .

The sample was processed using a cross-hatching scanning strategy in a bidirectional manner to process a surface area of  $4 \times 4 \text{ mm}^2$  by laser ablation to create cross-hatched patterns in ambient air according to selected laser parameters. The scanning patterning design was done by Direct Machining Control (DMC) 1.7.60 (64bit) software (Direct Machining Control, UAB, Vilnius, Lithuania) and the laser processing scheme is shown in Figure 1. The detailed laser input parameters used in the laser structuring are found in Table 1. In this cross-hatching scanning strategy, the first scanning was done in a direction at an angle of  $45^\circ$  and the second scanning at an angle of  $135^\circ$  to create a cross-hatched grid pattern (SEM images showing the pattern are shown in Figure S1 (Supplementary Information)). The laser beam was moved on the surface at a specified hatching distance, H, and a scanning velocity, V, during the raster scanning of the sample and in bidirectional scan trajectories. From Table 1, the pulse overlap (PO) for regions 1, 2, 3, and 4 was 93, 90, 87, and 73% respectively, while the scanning line overlap (LO) was 80, 0,  $-60$  and  $-100\%$ , respectively [32]. After laser processing, the sample was cleaned using pressurized air only.

**Table 1.** Experimental design used for laser processing of CP Ti sample.

Regions	Laser Fluence, $[\text{J}\cdot\text{cm}^{-2}]$	Scanning Velocity, $[\text{mm}\cdot\text{s}^{-1}]$	Hatching Distance, $[\mu\text{m}]$	Scanning Passes,	Regions	Laser Fluence $[\text{J}\cdot\text{cm}^{-2}]$	Scanning Velocity $[\text{mm}\cdot\text{s}^{-1}]$	Hatching Distance $[\mu\text{m}]$	Scanning Passes
A1	0.2	100	5	1	C3	1	200	40	4
A2	0.2	150	25	2	C4	1	400	50	8
A3	0.2	200	40	4	D1	1.2	100	5	1
A4	0.2	400	50	8	D2	1.2	150	25	2
B1	0.5	100	5	1	D3	1.2	200	40	4
B2	0.5	150	25	2	D4	1.2	400	50	8
B3	0.5	200	40	4	E1	1.5	100	5	1
B4	0.5	400	50	8	E2	1.5	150	25	2
C1	1	100	5	1	E3	1.5	200	40	4
C2	1	150	25	2	E4	1.5	400	50	8

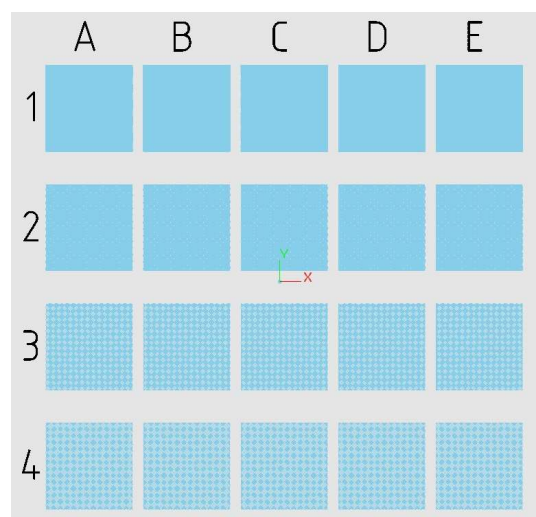


**Figure 1.** Laser processing scheme of the CP Ti.

The surface morphologies of the polished sample and the laser-processed regions were evaluated using a scanning electron microscope (SEM, MIRA, Tescan, Brno-Kohoutovice, Czech Republic) using secondary electrons. The sample was examined using a 5 kV accelerating voltage. Measurements of the periodicity and dimensions of micro/nanostructures on the sample surfaces were estimated from SEM images by the free image processing software ImageJ 1.54 g and the average of the measurement values are presented herein. The morphology was assessed also after immersion of the laser-structured sample in seawater from the Caspian Sea for 14 days to check if there were morphological changes after immersion. An energy-dispersive X-ray spectrometer (EDX, Oxford Instruments, Oxford, UK) attached to the MIRA SEM was used for elemental quantification of the CP Ti. The regions were examined using a 20 kV accelerating voltage and beam intensity (BI) index of 16.5 and both secondary electrons and backscattered electrons were collected.

A surface profilometer (Dektak XT, Bruker, Billerica, MA, USA) was used to profile surface topography and determine surface-based roughness parameters of the laser-structured surfaces. The profiler has a vertical resolution of 1 Å and the tip used has a radius of 2 μm. The open-source Gwyddion 2.64 programme was used to evaluate the collected data. Optical observations were performed with a stereomicroscope (Stemi 508, Zeiss, Oberkochen, Germany) on the laser-ablated regions. The laser-structured areas were illuminated perpendicularly with full-intensity LED illumination. Observations of the colours were made from one direction and an Axiocam 105 colour camera was used to record optical images for analysis.

The wetting behaviour of the laser-structured surfaces of the CP Ti was evaluated using contact angle (CA) measurements using the sessile drop method (See System E, Advex Instruments, Brno-Komín, Czech Republic) at 22 degrees Celsius. In the sessile drop method, 3.0 μL droplets of distilled water were placed on the laser-structured surfaces in an ambient environment. The 3.0 μL droplet was used because it experienced less gravitational forces [28]. The circle fitting mode was used to calculate the average contact angles. The CAs measurements were determined after two months after laser ablation to ensure the achievement of steady-state values of the CAs measurements [33]. After measuring the CAs, the laser-structured sample was immersed in seawater collected on 19 November 2023 from the Caspian Sea for 14 days. This was to understand the effects of immersion on the wettability of the laser-structured CP Ti sample in salty seawater. The properties of the Caspian Sea water can be found in the literature [34,35]. The immersed sample was thereafter subjected to wettability tests immediately after immersion. After immersion, the immersed sample was left in ambient conditions before being subjected to wettability tests again after 10 days. The aim of performing CA measurements after 10 days was to try to establish if hydrophobicity could be attained 10 days following immersion. Determination of the surface free energies (SFEs) at the laser-structured surfaces was based on the Li–Neumann model which requires only one liquid with known surface tension to be used [28,36,37]. In our study, distilled water with known surface tension of 72.83 mJ/m<sup>2</sup> at 20 °C was used [38].

A Raman confocal microscope (Alpha300R, Witec, Ulm, Germany) was used to perform the Raman measurements to analyse the surface oxide phases present after laser processing. For comparison purposes, the Raman spectrum of the polished surface of the CP Ti was also measured. The microscope has a motorised X-Y-Z stage and an objective lens of X100 was used. The laser source selected had a 532 nm excitation wavelength and a laser power of 25 mW was used. Prior to measurements, a silicon wafer with a particular Raman peak at 520 cm<sup>-1</sup> was used to check the calibration of the Raman microscope. Within a spectral range of 1146 cm<sup>-1</sup> to 0 cm<sup>-1</sup>, 50 accumulations were measured with a 5 s integration time to obtain the Raman spectra. The resolution of the measurements was 1 cm<sup>-1</sup>. Raman measurements were acquired using WITec Project FIVE 5.1.8.64 proprietary software and processed using OriginPro 8.5.0 SR1 proprietary software (OriginLab Corporation, Northampton, MA, USA). Raman measurements were made after immersion of the sample in seawater.

### 3. Results and Discussion

This study aimed to investigate the influence of laser processing parameters on the development of different morphologies, topographies, surface chemistry, colourization, and wettability after laser structuring using a picosecond laser. Therefore, the areas of  $4 \times 4 \text{ mm}^2$  on the CP Ti were laser-structured in raster-scanning mode under four laser processing parameters.

#### 3.1. Morphology of the Laser-Processed Surfaces

Prior to laser structuring, the sample was mechanically polished to obtain a smooth and clean surface with no inclusions or surface structures as seen in the SEM image in Figure 2 (labelled Ti). Then, different regions on the CP Ti sample were laser-structured with a pulsed picosecond laser to generate micro-/nanostructures with different input laser processing parameters. During laser processing of any material, unique surface structures referred to as laser-irradiated periodic surface structures (LIPSSs) [18] are generated when the ablation fluence just exceeds the ablation threshold [31]. The removal of materials in pulsed laser processing is facilitated by a single Gaussian-shaped pulse. The pulse energy  $E$ , and by extension average laser power  $P$ , of a single Gaussian laser pulse are associated with the peak laser fluence  $F_p$  through the relationship given in (1):

$$F_p = \frac{2E}{A} = \frac{2E}{\pi\omega_0^2} = \frac{2P}{\pi\omega_0^2 f} \quad (1)$$

where  $A$  is the focused area on the surface of the substrate,  $\omega_0$  is the spot radius and  $f$  is the repetition rate.

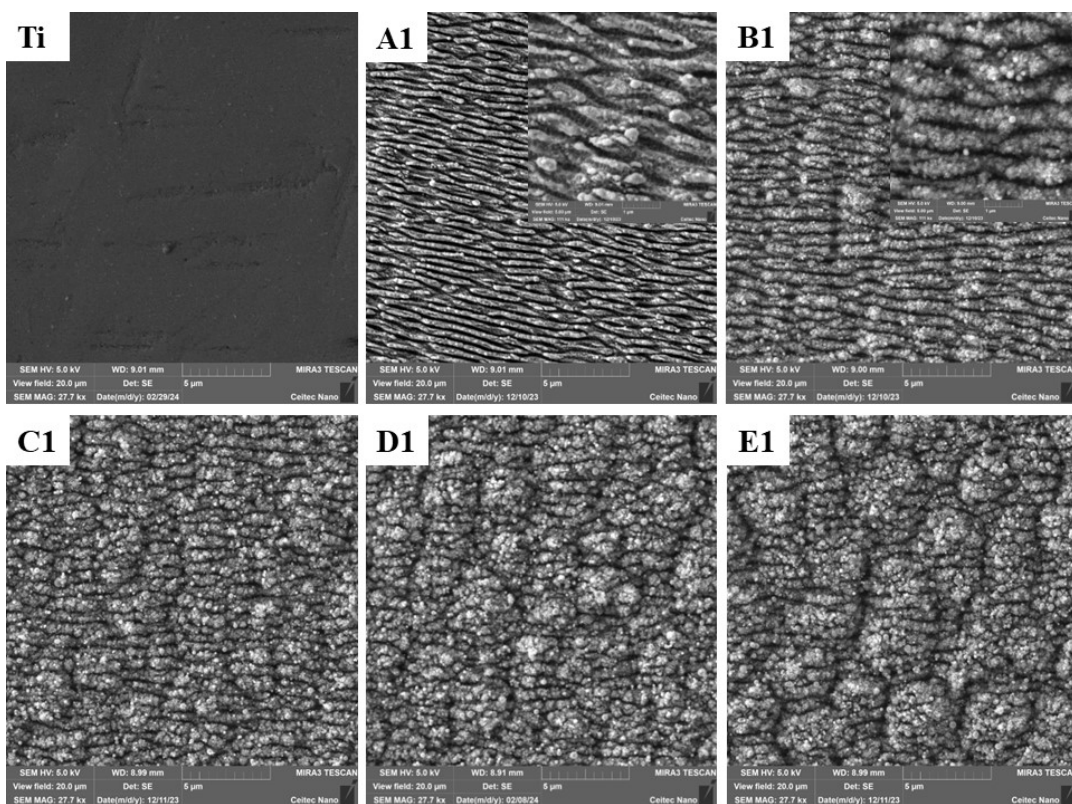


**Figure 2.** SEM micrographs of ps laser-structured CP Ti surfaces showing LIPSS produced on regions A1, B1, C1, D1, and E1 using laser fluence of  $0.2 \text{ J/cm}^2$ ,  $0.5 \text{ J/cm}^2$ ,  $1 \text{ J/cm}^2$ ,  $1.2 \text{ J/cm}^2$ , and  $1.5 \text{ J/cm}^2$ , respectively.

The surface morphology of the regions on the laser-structured sample is shown in Figure 2. Under laser structuring, the CP Ti material undergoes structural changes, forms

surface structures, and becomes rough. Figure 2 shows SEM images at the surfaces of the laser-structured CP Ti after laser ablation with ps laser pulses at various laser fluences of 0.2, 0.5, 1, 1.2, and 1.5 J cm<sup>2</sup> at regions A1, B1, C1, D1, and E1, respectively. A 100 mm/s scanning velocity, 5 μm hatching distance, and single scanning pass were used to process these five regions. The morphology of the surface nanostructures was determined using SEM without encountering any charging effects. This means that the oxide layer on the surfaces of the laser-structured regions was thin and, hence, could not have the charging effects normally encountered with thick titanium oxide [27]. At these regions, the PO and the LO were 93% and 80%, respectively [32], and this ensures that the laser pulses remove the material to form a shallow square cavity. At these five regions, the effective pulse number,  $N_{\text{eff}}$ , per focussed diameter ( $N_{\text{eff}} = \frac{D \times f}{V}$ ) which facilitates the ablation process was 15 pulses [32].

As shown in Figure 2 the ablated part on region A1 has smooth and well-formed LIPSS. The LIPSSs formed had an average periodicity of approximately 462 nm and were oriented perpendicular to the laser beam polarization [18,39]. Because the laser wavelength,  $\lambda$ , is substantially longer than the periodicity,  $\Lambda$ , ( $\lambda/2 > \Lambda$ ) of this type of LIPSS, it is called high spatial frequency LIPSS (HSFL) [39,40]. The valleys of the LIPSS on region A1 (Figure 2, Inset on A1 region) are decorated by threadlike nanostructures that are oriented perpendicular to the HSFL. The ridges of the LIPSS on region A1 have been decorated by a few nanodroplets [24].

In Figure 2, the ablated part in region B1 has less smooth LIPSS than in the A1 region. These LIPSS have narrow valleys in comparison to those in the A1 region. The average periodicity of the LIPSS is 722 nm. This type of LIPSS is considered as low spatial frequency LIPSS (LSFL) because the laser wavelength,  $\lambda$  is longer than the periodicity,  $\Lambda$ , ( $\lambda/2 < \Lambda$ ) of this type of LIPSS, and its orientation is perpendicular to the laser beam polarization [18,39]. The ridges of the LIPSS are decorated by cloudy-like nanostructures and a few nanodroplet materials as seen in the Inset on B1 region in Figure 2 and can be considered nanostructured-covered LIPSS (NC-LIPSS) [41]. At the region C1 region, the ablated region is covered by less smooth and shorter NC-LIPSS than that in the B1 region, as seen in Figure 2). The valleys of these NC-LIPSSs are much narrower than those in the B1 region and their average periodicity is 727 nm and hence considered as LSFL. The NC-LIPSSs are decorated by a few nanodroplet materials. Irregular micro-ripples appear to be starting to form on the surface along the scanning direction [25]. At regions D1 and E1, the NC-LIPSS are poorly formed, decorated by a few nanodroplet materials and irregular micro-ripples are formed as seen in Figure 2. The average periodicity of these NC-LIPSSs is 735 nm and 764 nm for regions D1 and E1, respectively, hence considered as LSFL. Micro-ripples in the E1 region are more visible than in region D1.

In these five regions, the ablated zones show no signs of molten material, according to the SEM images in Figure 2, showing that equilibrium vaporisation (gentle ablation phase) was the ablation mechanism in these regions [42]. The ablation rate  $d_a$  was low due to the low laser fluence employed, and it was dependent on the optical penetration depth, as shown in (2) [28,43]:

$$d_a = \alpha^{-1} \ln\left(\frac{F_p}{F_{t,g}}\right) \quad (2)$$

where  $\alpha^{-1}$  is the optical penetration depth,  $F_p$  is peak laser fluence and  $F_{t,g}$  is the single-pulse ablation threshold fluence.

From the SEM images in Figure 2, the LIPSS formed have different morphology with a different periodicity. This is because they were processed by different laser fluences which depend on the pulse energy of the laser pulse. Laser fluence increases with pulse energy, according to (1). As a result, more energy is deposited to the substrate, causing different LIPSSs with different morphologies to form. In general, HSFLs are formed at low fluence regimes, whereas LSFLs become more noticeable at higher fluence levels. Additionally, the periodicity of the LIPSS increases as the laser fluence increases. Additionally, it was

observed that, as laser fluence rises, LIPSSs become discontinuous and are decorated by nanodroplets.

The SEM micrographs of the laser-structured surfaces at 100, 150, 200, and 400 mm/s scanning velocities in the regions indicated on each image are displayed in Figure 3.

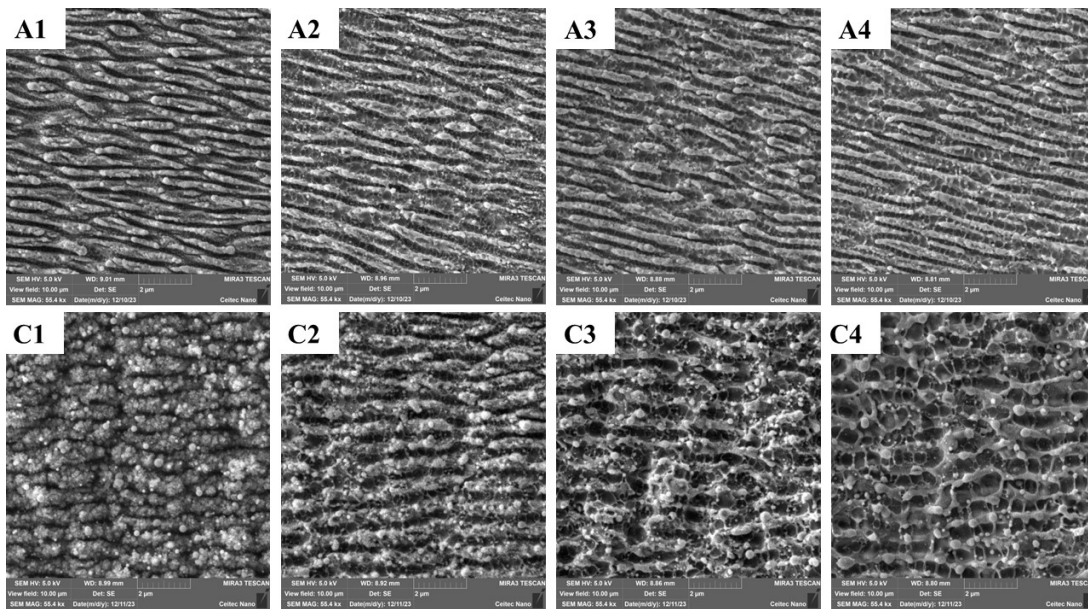


**Figure 3.** SEM micrographs of ps laser-structured CP Ti surfaces of regions shown on each micrograph. The laser processing parameters indicated in Table 1 were used to process these regions.

In these regions, there is the formation of LIPSSs in a perpendicular direction to the laser polarization. In Figure S1, it can be noted that the LIPSSs are formed over the whole surface of region A1, while in regions A2, A3, and A4, the surface is made up of the laser-structured areas covered with LIPSS and unstructured square areas in an alternating manner due to the hatching distance of 25 µm, 40 µm, and 50 µm, respectively. The average periodicity of the LIPSSs was 476 nm, 456 nm, 449, and 439 nm for regions A1, A2, A3, and A4, respectively, hence considered as HSFLs [39]. It can be noted in Figure 3 that, as scanning velocity or hatching distance increases, the formation of threadlike nanostructures along the valleys of the LIPSS that are perpendicular to the LIPSS becomes more evident. This can be noted in the A4 region, where LIPSSs are decorated by threadlike nanostructures along the valleys.

In the C1, C2, C3, and C4 regions in Figure 3, there is also the formation of LIPSSs. In Figure S1, C1 and C2 regions are covered by LIPSS while C3 and C4 regions have some unstructured areas while structured areas are covered by LIPSS. At the C1 region, LIPSS is poorly formed and is nanostructured, hence referred to as NC-LIPSS and irregular micro-ripples are seen. In the C2 and C3 regions, the LIPSSs formed are more visible than in the C1 region. Along the valleys of the LIPSS in the C3 and C4 regions, threadlike nanostructures are being formed, which are in a perpendicular direction to the LIPSS. In the C4 region, threadlike nanostructures along the valleys are more evident than in the C3 region.

The differences in the morphologies of the surfaces as depicted in Figure 3 suggest that the scanning velocity and/or hatching distance affect each irradiation process on each region. The POs, due to the different scanning velocities used on A1/C1, A2/C2, A3/C3, and A4/C4 regions, were 93, 90, 87, and 73%, respectively, while  $N_{eff}$ , which facilitates the ablation process, were 15, 10, 8, and 4 pulses, respectively [32]. These changes in POs or  $N_{eff}$  led to varying heat energy deposition on each surface of the region, which in turn produced varying surface nanostructures with varying morphologies in each region [44]. From the discussion, it has been established that laser fluence, scanning velocity, and hatching distance influenced the formation of LIPSSs and affected their morphology [9].

We find that the periodicity of the LIPSS is directly dependent on the laser fluence and scanning velocity.

The LSFLs are formed as a result of the interference of incident laser with scattered or excited tangential surface waves or surface plasmons which results in a spatially periodic energy distribution on the surface [45–47]. The formation mechanism of the HSFL has not been agreed upon by researchers and several theories have been put forward such as self-organization, and a second and third harmonic generation (SHG, THG), among others [18,40,46].

After immersion of the laser-structured sample in seawater, the morphology of the sample was determined again using SEM. The aim was to check if there were possible morphological changes after immersion in seawater. It can be noted from Figure S2 (Supplementary Information), that there were no major changes in the morphology of the A1, B1, C1, D1, and E1 regions. The LIPSS as observed have become clearer in comparison to the ones observed in Figure 2. This might be a result of the removal of some ablation debris particles by seawater after immersion. The dimensions of the LIPSS remained almost the same and this shows that the LIPSS formed has good structural stability when exposed to a salty environment caused by seawater.

### 3.2. Topographical Analysis of Laser-Structured Surfaces

Prior to laser structuring, the sample was mechanically polished to obtain a smooth and clean surface. The polished surface of CP Ti had an average surface roughness,  $S_a$ , of  $\sim 15$  nm. During laser processing using various laser processing parameters, different surface structures with various topographies are generated on the CP titanium. Figure 4 shows the topographical images of the laser-structured surfaces at A1, B1, C1, D1, E1, D4, and E1 regions obtained after laser ablation. It can be noted from Figure 4 that all surfaces of the laser-structured parts are rough. The A1 region (Figure 4a) shows that the surface structures do not have a lot of protrusions in comparison to the other four regions. In the B1, C1, D1, and E1 regions, the surface structures have numerous small protrusions. In D4, there are unprocessed and processed parts where the laser beams pass during scanning. The processed part is made up of almost V-shaped micro-grooves with a top width of  $\sim 27$   $\mu$ m and depth of  $\sim 1.09$   $\mu$ m. The unprocessed part remained because the hatching distance used could not facilitate the line overlapping (LO =  $-100\%$ ) of the laser tracts.

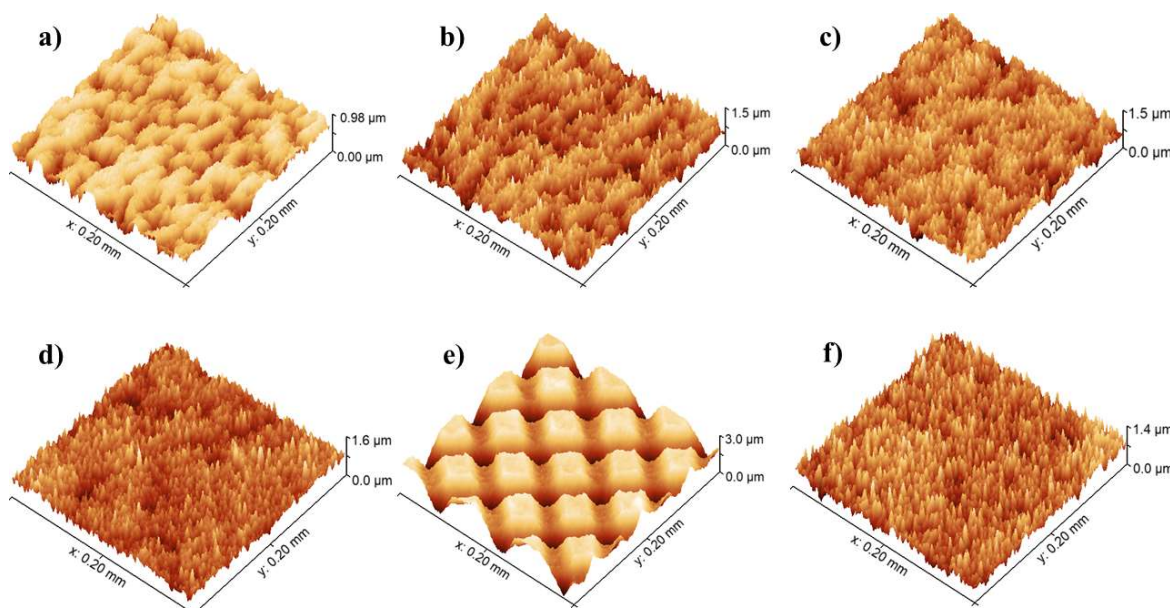


**Figure 4.** Topography of the laser-structured CP Ti on the: (a) A1, (b) B1, (c) C1, (d) D1, (e) D4, and (f) E1 regions.

The area parameters, such as surface roughness  $S_a$ , skewness  $S_{sk}$ , kurtosis  $S_{ku}$  and surface slope  $S_{dq}$ , were determined using Gwydion 2.64 software and tabulated in Table 2. The  $S_a$  values obtained were on the nanoscale and this is due to the low laser fluence used which did not ablate the material deeply in the ablation process. Most of the  $S_{sk}$  values are less than zero ( $S_{sk} < 0$ ), meaning that there were more valleys than peaks in processed regions [17,28]. For the  $S_{ku}$  values, all regions have features with peaks and valleys which are not sharp ( $S_{ku} < 3$ ) [17,28]. The  $S_{dq}$  values are very small, showing that the degree of openness of the surfaces in all directions is low. Observation from Table 2 shows that  $S_{dq}$  increases with increasing laser fluence.

**Table 2.** Surface roughness values of the laser-structures regions of CP Ti.

Regions	Mean Roughness $S_a$ (nm)	Skewness, $S_{sk}$	Kurtosis, $S_{ku}$	RMS Surface Slope, $S_{dq}$	Projected Area ( $\mu\text{m}^2$ )	Surface Area, ( $\mu\text{m}^2$ )	Roughness Factor, $r^*$
A1	118.2790	-0.7021	-0.0444	0.0834	40,006.7000	40,138.8000	1.0033
B1	157.3180	-0.3043	-0.0626	0.1375	40,006.7000	40,362.3000	1.0089
C1	136.5680	-0.2754	0.2999	0.1376	40,006.7000	40,363.3000	1.0089
D1	127.0170	0.1471	0.7541	0.1531	40,006.7000	40,447.4000	1.0110
D4	510.3000	-0.4424	-0.6126	0.1316	40,007.0000	40,341.0000	1.0083
E1	136.7490	0.2370	0.1862	0.1766	40,006.7000	40,592.7000	1.0146

\* Calculated value.

### 3.3. EDX Analysis

The amount of elements present on the surface and below the surface of a sample varies when it is subjected to laser ablation. To ascertain the influence of laser processing on the elemental composition of the CP Ti sample, EDX measurements were undertaken before and immediately after immersion and compared with the polished sample. The EDX data from the measurements are tabulated in Table 3. The EDX data from the polished sample and laser-processed CP Ti samples shows that the elements consist mostly of Ti, and small quantities of O, C, Fe, and Al. The percentage composition of Ti is highest in the polished CP Ti in comparison to the laser-structured regions of the CP Ti. This shows that Ti exists as elemental Ti on the surface of the polished sample. The percentage composition of oxygen on the polished CP Ti appears higher than the value in the literature because, after polishing, the oxygen in the air may have reacted readily with titanium to form a very thin natural oxide layer [48].

**Table 3.** Average elemental composition (wt. %) in the sample's regions.

	Elements (% Weight)									
	Before Immersion					After Immersion				
	Ti	O	C	Fe	Al	Ti	O	C	Fe	Al
Polished	99.1	0.7	0.1	0.1	0.1	91.5	8.2	0.0	0.1	0.1
A1	90.1	9.6	0.1	0.1	0.1	91.3	8.6	0.0	0.0	0.1
A4	91.9	7.4	0.4	0.2	0.1	89.3	10.5	0.1	0.0	0.0
B1	89.1	10.6	0.1	0.1	0.1	89.0	10.8	0.0	0.0	0.1
C1	88.8	10.9	0.1	0.1	0.1	88.9	10.8	0.0	0.1	0.1
D1	88.5	11.2	0.1	0.1	0.1	87.1	12.8	0.0	0.1	0.1
E1	86.9	12.9	0.1	0.1	0.0					

Table 3 illustrates how the elements' compositions vary after laser processing. It can be noticed that the quantity of Ti element has reduced after laser processing in ambient conditions while the O element has increased. Ti has decreased in amount because titanium oxides are formed on the surface of the sample as a result of the elemental Ti's oxidation reaction with oxygen facilitated by laser ablation [9,46,49–51]. Following laser ablation, titanium oxides have formed on the surface, increasing the amount of oxygen on the

surface [51,52]. The amount of C remained the same as before laser structuring because the storage period of two months enabled the laser-structured surfaces to have organic hydrophobic C functional groups adsorbed on them [17,51,53].

The amount of Ti in A1 is less compared to in A4 while the amount of O is higher in A1 than in A4. The two regions were processed differently based on the hatching distance and scanning velocity. The PO and LO were 93% and 80%, respectively, in the A1 region, and 73% and –100%, respectively, in the A4 region [32]. Consequently, different heat energy depositions occurred on each surface, with a greater amount of heat energy being deposited in the A1 region compared to the A4 region. Consequently, the A1 region experienced a greater degree of Ti oxidation than the A4 region.

From Table 3, it can be noted that the amount of Ti reduces as the amount of laser fluence is increased. This indicates that Ti is oxidised more as laser fluence increases. Additionally, from Table 3, it can be noted that the amount of O increases as laser fluence increases because of the formation of greater quantities of the thin layer of oxide film on the surfaces. The increment of the O could also be associated with the availability of more pockets of air on the rough surfaces generated by laser structuring [32].

By comparing the elements in the regions before and after immersion in seawater, it can be noted that the amount of Ti has increased, while C and O have reduced. This could be attributed to the removal of some ablation debris particles by seawater after immersion as was noted through the comparison of SEM images in Figures 2 and S2. The ablation debris on the surfaces of the material could have had some more accumulated oxygen in the form of oxides on its porous surface. The removal reduces the quantity of the oxide layer and exposes more of the titanium element. The absence of the carbon element on the immersed sample is that it is likely to have been desorbed from the laser-ablated surface after immersion.

### 3.4. Raman Analysis

Surfaces of regions A1, B1, C1, D1, and E1 of the laser-processed Ti were analyzed using Raman microscopy to understand the influence of laser structuring on the formation of surface oxide phases on titanium alloy [9]. To bring out this influence clearly, the Raman spectrum of the polished CP titanium surface was also measured. When metals are processed by laser, there is a formation of oxides on the surface [49]. Raman is widely used to characterize transition metal oxide structures present on the surface because it is sensitive to metal oxide vibrations [54]. It is expected that there was a formation of titanium oxides on the surface after laser ablation in ambient conditions [9]. Titanium oxide phases are Raman active between  $100\text{--}900\text{ cm}^{-1}$  regions [55]. The rutile and anatase phases have four ( $A_{1g}$ ,  $B_{1g}$ ,  $B_{2g}$ ,  $E_g$ ) and six ( $1A_{1g}$ ,  $2B_{1g}$ ,  $3E_g$ ) active modes with symmetries, respectively, which occur at a certain Raman shift [56]. The Raman spectra of the polished surface and the surfaces structured by a laser before immersion and after immersion in seawater are shown in Figure 5.

It can be observed that the spectrum of the polished surface of the CP Ti has no notable peaks, while the spectra of the laser-structured surfaces have pronounced peaks [27]. The absence of notable peaks for polished CP Ti shows that its surface had only the naturally occurring thin oxide film. This corroborates the EDX findings that the polished CP Ti surface has elemental Ti as the main element (~99.1%). It can be noted that the spectra have peaks at various Raman shifts and with various intensities which depend on the oxide crystallinity formed during laser processing [55]. The Raman spectra of the surfaces of the regions before and after immersion in seawater have four peaks labelled P1, P2, P3, and P4, but, on the A1 region before immersion in seawater, peak P1 was not well resolved. Since the Raman peaks in Table 4 exhibit strong agreement with reference values for the rutile phase of the  $\text{TiO}_2$  [56,57], they have been allocated to various vibration modes based on their positions in the spectra.

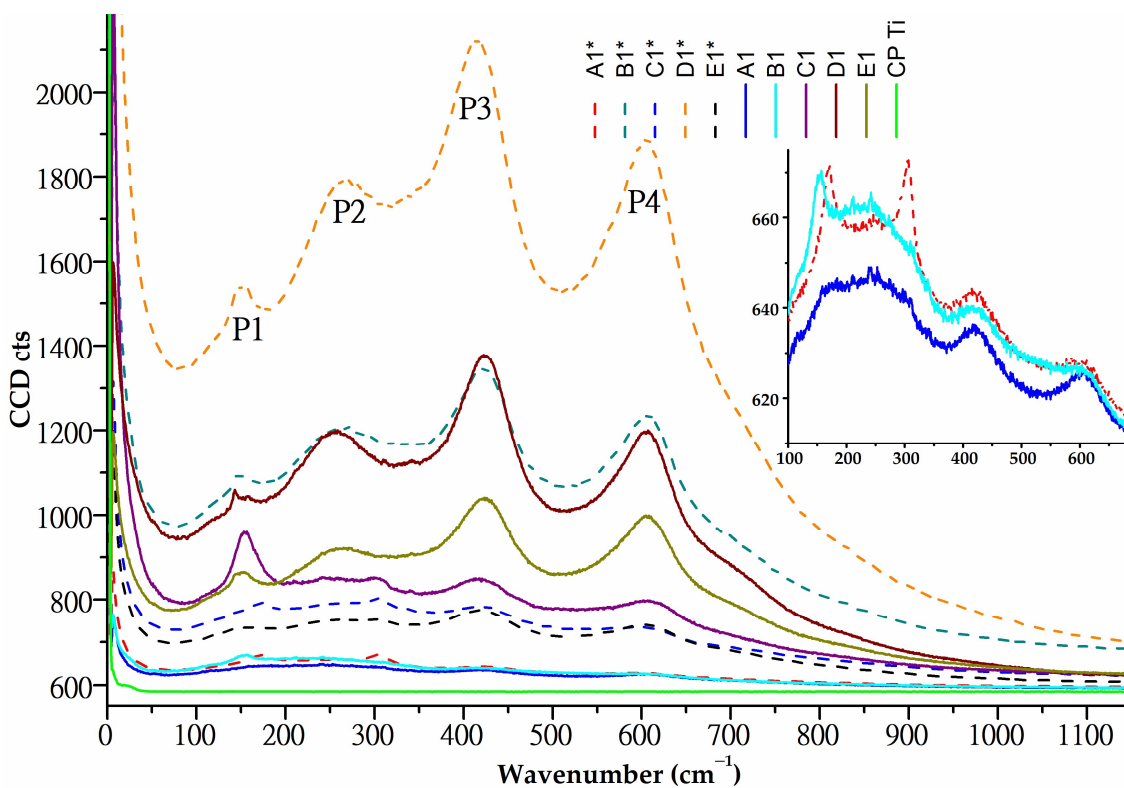


**Figure 5.** Raman spectra of the polished CP Ti and the laser-structured CP Ti showing different peaks on the surfaces of A1, B1, C1, D1, and E1 (before immersion) and A1\*, B1\*, C1\*, D1\*, and E1\* regions (after immersion).

The most intense peaks, P3 and P4 (Figure 5), for the five regions which have been assigned to  $E_g$  and  $A_{1g}$  respectively confirm that the oxide phase formed on the surfaces was mostly that of rutile [55,58].  $B_{1g}$ ,  $E_g$ , and  $A_{1g}$  modes are associated with symmetric bending, symmetric stretching, and antisymmetric bending vibrations of O-Ti-O bonds, respectively [55].

Surfaces in the regions D1 and E1 before immersion in seawater have sharp peaks P3 and P4, with high intensities. This signifies that the amount of the oxide phases formed in these two regions is higher than in regions A1, B1 and C1 [55]. The higher intensities mean that the higher the laser fluence used, the higher the amount of the oxide phase formed on the surface.

Through comparison of the peak positions of the regions before and after immersion in Table 4, it can be noted that the peak positions did not change much. Some peaks redshifted while others blueshifted and this could be attributed to the dimensional changes of the surface nanostructures on the laser-structured CP Ti material [22].

**Table 4.** Positions of Raman peaks on the surfaces of the laser-structured CP Ti.

Peaks	Before Immersion					After Immersion					Assigned Mode
	A1	B1	C1	D1	E1	A1	B1	C1	D1	E1	
P1	153	157	154	143	154	169	151	167	151	154	$B_{1g}$
P2	242	242	242	259	266	246	264	254	272	261	Multi-photon process
P3	417	418	419	422	423	420	420	417	415	416	$E_g$
P4	608	605	609	608	605	597	609	603	604	606	$A_{1g}$

### 3.5. Optical Observations of the Laser-Structured Surfaces

One of the objectives of the study was to study colours formed when laser processing parameters are varied. The laser fluence used ( $0.2\text{--}1.5\text{ J/cm}^2$ ) was intended to create LIPSSs, also known as ripples. Figure 6 displays the optical observations obtained from the CP Ti's laser-ablated surfaces under the same viewing conditions. It can be observed that the various colours produced on the surfaces of the laser-structured CP Ti depend on the laser processing parameters tabulated in Table 1.

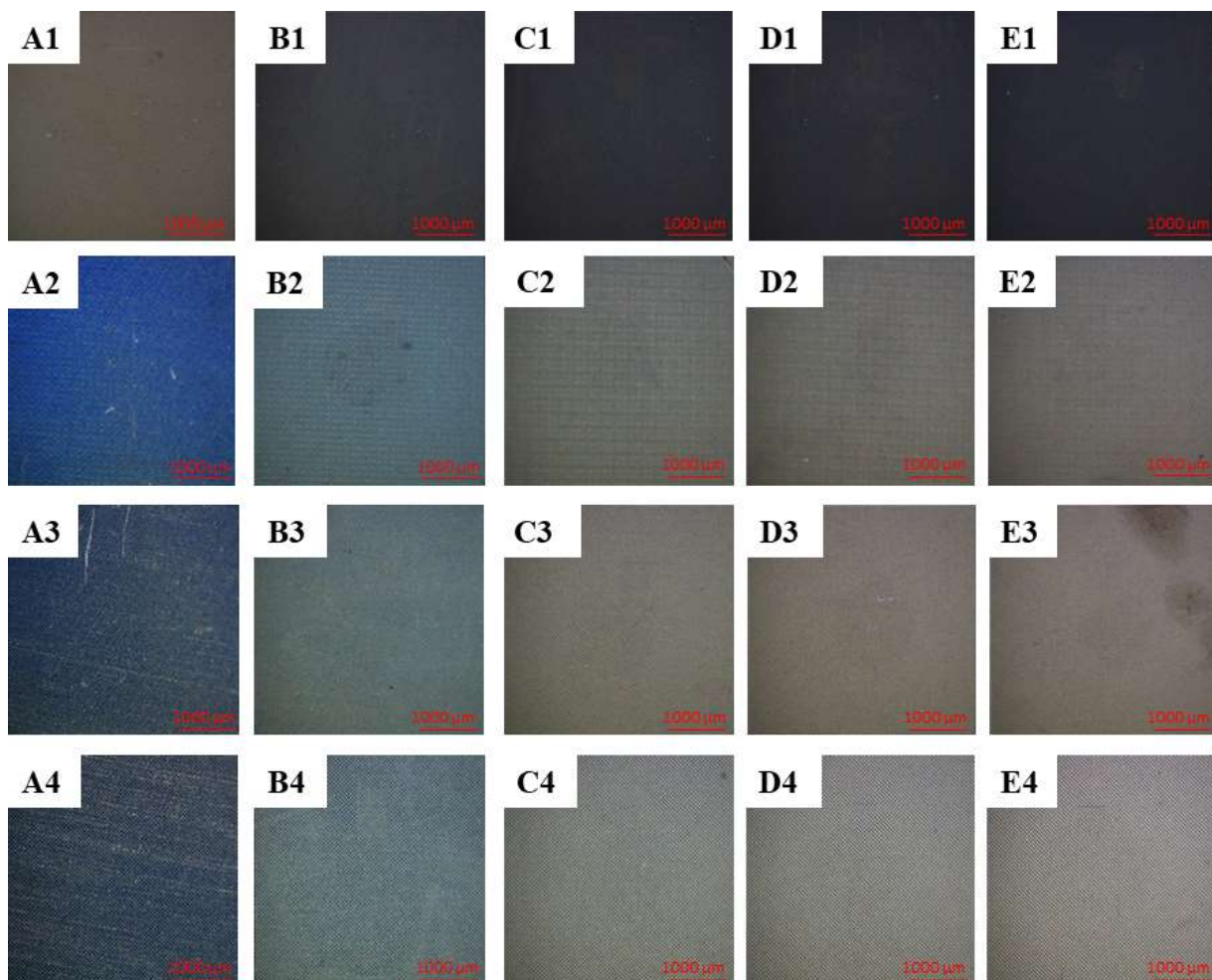


**Figure 6.** Optical images of the different regions (A1–E4) of the CP Ti after ps laser processing in scanning mode. The regions were processed using the laser processing parameters in Table 1.

It can be noted from Figure 6 that surfaces processed by lower laser fluences have more saturated colours than those processed by a higher laser fluence. This can be seen in Figure 6, where the A1 region has a taupe grey colour while the B1 region has a steel grey colour. It has been discussed that the colours formed on the surfaces of the metallic substrate can be attributed to the LIPSS, oxides, or optical active nanostructures formed after laser processing [22]. Through examination of the SEM images in Figures 2 and 3, it can be noted that the surface structures formed varied depending on the laser processing parameters.

From Figure 2, region A1 is composed of well-formed LIPSS with a periodicity of 462 nm, while regions B1, C1, D1, and E1 are composed of NC-LIPSS with a periodicity of 722 nm, 727 nm, 736 nm, and 764 nm, respectively. Therefore, the variation of the morphologies of the LIPSS and NC-LIPSS brings the different grey colours observed in the first row in Figure 6. It can be observed from row one in Figure 6, that the intensity of the grey colours increases as the laser fluence increases. This could be explained by the changes

in the periodicity of the LIPSS, as has been explained by Li et al. [21]. The greyish colour observed in regions A1, B1, C1, D1, and E1 could be attributed to multiple scatterings of the white light by nanostructures decorating the LIPSS [22].

It can be observed that colours vary in tandem with changes in scanning velocity, hatching distance, and number of scanning passes [44]. This can be seen in Figure 6, where, in region A1, the surface has a taupe grey colour, while in regions A2, A3, and A4, the blue colour changes its saturation level as the levels of the laser parameters change. This can be explained by examining the SEM images in the first row in both Figures 3 and S1. In the first row in Figures 3 and S1, it can be noted that the LIPSSs are formed over the whole surface of region A1, while in regions A2, A3, and A4, the surface is made up of the laser-structured areas covered with LIPSS and unstructured square areas in an alternating manner due to the hatching distances of 25  $\mu\text{m}$ , 40  $\mu\text{m}$ , and 50  $\mu\text{m}$ , used, respectively. As the hatching distance increases, the unprocessed square areas increase, and the intensity level of the bluish colour reduces. This shows that hatching distance plays a critical role in the colourization of the surfaces. The bluish colour observed in regions A1, A2, A3, and A4 could be attributed to the presence of well-ordered LIPSS which acts as optical surface diffraction gratings [21,22].

From Figure 6, regions C2, D2, and E2 have the same colour. Similarly, the set of regions C3, D3, and E3 and regions C4, D4, and E4 have the same colour. By observing the SEM images of these regions in Figure S1, the morphologies of each set of regions are almost identical. These similar morphologies could be responsible for the similar colours observed.

The colours observed on the surfaces of the laser-ablated regions by the ps laser can be a result of inherently generated periodic surface structures on the material which cause optical diffraction effects and are referred to as structural colours [22,24]. These periodic surface structures diffract incident light in separate directions according to their different wavelengths [20]. This diffraction generates a colourization effect on the laser-structured surfaces. This variation of structural colours on the laser-structured regions indicates that the surface structures present have different types of morphologies with different dimensions depending on the laser processing parameters [27].

It has also been published that the oxide films formed on the surface of the titanium play a role in colourization due to thin oxide film interference [7,22]. When incident white light is illuminated on the laser-structured surfaces, reflection from the sides of the oxide film will happen and, in case of the interference of the reflected lights, the colourization effect will happen [20]. From the EDX analysis, it was noted that there was a formation of thin oxides on the surface of CP Ti after laser processing. Similarly, Raman's analysis established that the rutile phase of  $\text{TiO}_2$  was present on the surface of the laser-processed CP Ti. The presence of a thin film of oxides on the surfaces of the laser-processed CP Ti implies that it could have contributed to the colourization of the laser-processed CP Ti [46]. The colour seen on the laser-structured surfaces depends on the thickness of the oxide, and the refractive index [20,22].

Barmina et al. [27] also explained that plasmon resonant oscillations of electrons in nanostructures bring about the colourization of Ti surfaces and these colours are commonly referred to as plasmonic colours. In ultrafast laser processing, the laser-induced nanostructures whose dimensions are less than the wavelength of incident light induce localized surface plasmon resonance (LSPR) [22]. This phenomenon happens when incident light causes the electrons at the nanostructure's surface to oscillate collectively, which enhances absorption and scattering at specific wavelengths [59]. These interactions depend on the wavelength of the incident light and the dimensions of the nanostructures [22].

Due to the existence of the LIPSS, the oxide layer, and nanostructures on the laser-structured surfaces of the CP Ti, it is difficult to determine the percentage contribution of the periodic surface micro-/nanostructures, oxide film, or nanostructures quantitatively to the final colour state of the laser-processed surface. Therefore, further research is recommended in this area.

### 3.6. Wettability Analysis on the Laser-Treated Surfaces

When a metal is subjected to laser ablation, its wetting properties are significantly modified. To understand the influence of laser processing on the wettability of pure titanium, contact angle (CA) measurements were determined two months after laser processing, before immersion, immediately after immersion, and 10 days after immersion. The CA of the polished CP Ti was measured to be about  $66^\circ \pm 5^\circ$  (and a sample image of the water droplet captured is shown in Figure 7a) and this exhibits the hydrophilic nature of the CP Ti [11,17,53]. Theoretically, immediately after laser structuring, Ti has hydrophilic behaviour, hence the need to wait for two months to obtain steady-state conditions for measurements of the CAs [33]. Sample images of water droplets on the laser-structured surfaces at the C3 region are shown in Figure 7. This illustrates how the contact angle for water droplets on laser-treated surfaces changes when exposed to different storage environments over time. The observations show that at the C3 region, the surface was in a hydrophobic, highly hydrophilic, and almost hydrophobic state two months after laser processing before immersion, immediately after immersion, and 10 days after immersion, respectively.

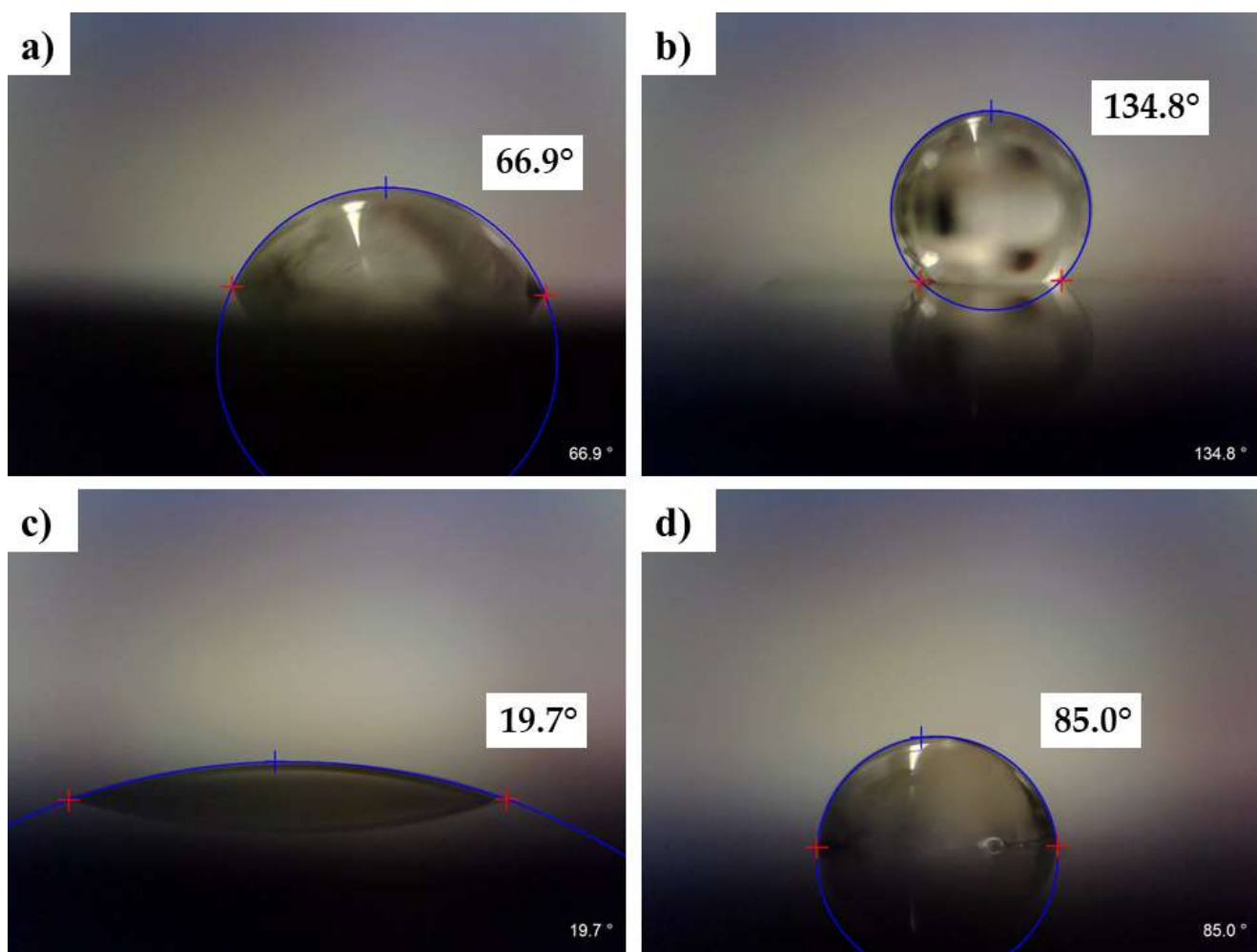


**Figure 7.** Water contact angle measurements on the (a) polished surface and the laser-structured surface at the C3 region, (b) two months before immersion, (c) immediately after immersion, and (d) 10 days after immersion.

The average CA measurements of the surfaces of the laser-processed CP Ti regions two months before immersion, immediately after immersion, and 10 days after immersion are plotted as shown in column green (CA 1), column red (CA 2), and column blue (CA 3), respectively, in Figure 8. Before immersion in seawater, as shown in the green column

(CA 1) in Figure 8, it can be noted that the CA measurements after laser processing have significantly increased as compared to the polished CP Ti surface. Except for the A4 region, which had a CA of roughly  $87^\circ$ , all regions processed by laser had CAs of  $\geq 91^\circ$ . This suggests that following laser processing the majority of the regions' surfaces were hydrophobic. Particularly in the regions of A1, B1, C1, D1, and E1, strong hydrophobicity was observed after processing at 100 mm/s, 5  $\mu\text{m}$  hatching distance, and one scanning pass.

Through comparison of the CAs of regions A1, B1, C1, D1, and E1 before immersion, as seen in Figure 8, it can be noticed that the CA increased as the laser fluence increased. However, CA in the A1 region was much lower in comparison to the other four regions. These variations of CAs point to different surface structures existing on the laser-structured surface. These surface structures exhibited various morphologies and topographies as shown in Figures 2 and 4, respectively. A1 is made up of entirely HSFL and has a CA of  $119^\circ$ , while B1, C1, D1, and E1 regions made up of NC-LIPSS have CAs of  $139^\circ$ ,  $139^\circ$ ,  $141^\circ$ , and  $143^\circ$ , respectively. Consequently, these surface structures have different roughness (Table 2), and this roughness influences the wettability.

It is evident from looking at the CAs in the C1, C2, C3, and C4 regions (Figure 8) that the CAs decrease with increasing scanning velocity and/or hatching distance. The CA values of the C1, C2, C3, and C4 regions, which were processed at a hatching distance of 5  $\mu\text{m}$ , 25  $\mu\text{m}$ , 40  $\mu\text{m}$ , and 50  $\mu\text{m}$ , were  $139^\circ$ ,  $137^\circ$ ,  $134^\circ$ , and  $127^\circ$ , respectively. Based on Figure S1, the morphologies of these regions vary. That means that the wettability will also vary depending on the surface structures present in each region. This signifies that regions subjected to short hatching distances will be more hydrophobic due to their rougher texture, and vice versa [28]. It was also noted during measurement before immersion that the wetting behaviour was isotropic, and this shows that wettability was independent of the morphological or ablations directions.

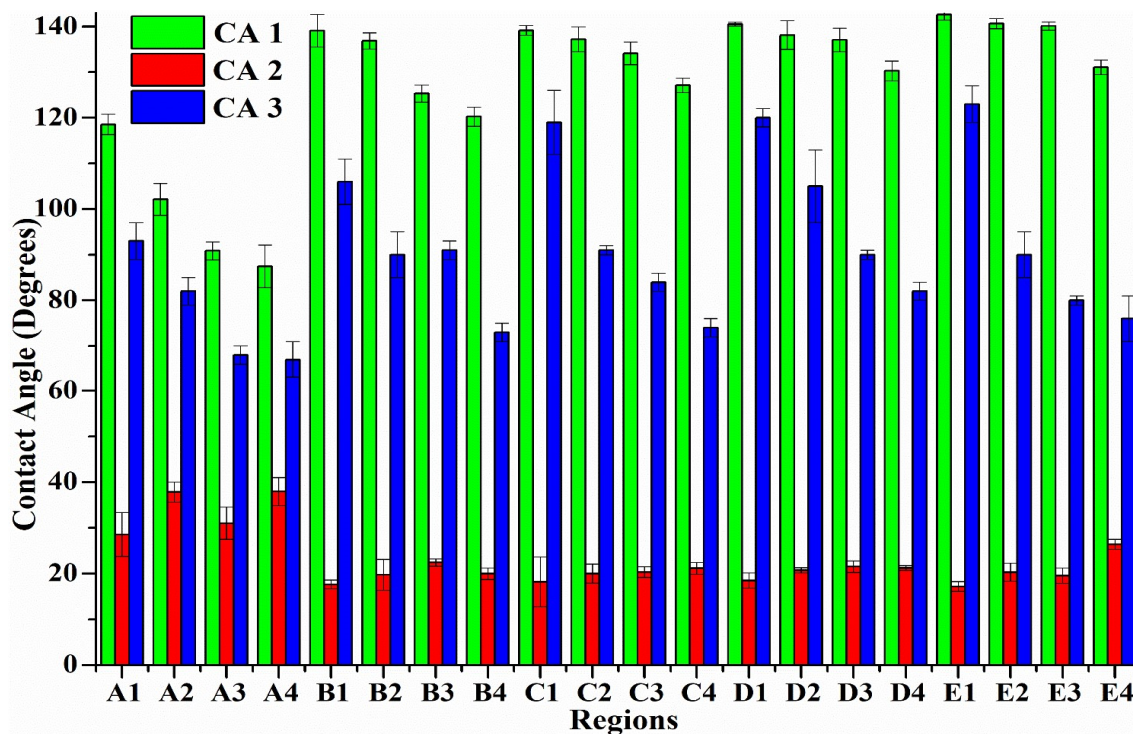


**Figure 8.** Average water contact angles on the surfaces of the laser-processed regions (A1–E4) of the CP Ti before immersion (CA 1), immediately after immersion (CA 2), and 10 days after immersion (CA 3).

Laser-processed surfaces become hydrophobic when measurements are performed two months after laser processing before immersion. This shows that a hydrophilic CP Ti material can be modified to become hydrophobic material through laser processing. The

wetting transition of the laser-structured CP Ti surfaces from a hydrophilic to a hydrophobic state is due to surface morphology/topography and surface chemistry [5,29,50,60]. Topography can be described by the shape profiles and roughness of a surface and the laser-processed surfaces have increased surface roughness caused by laser ablation [5], as noted in Table 2. The wettability transition due to roughness can be explained by the Cassie–Baxter theory [17,61,62] through a modified Cassie–Baxter equation, as shown in (3) [29,63–65]:

$$\cos \theta_{CB} = rf_{SL}\cos \theta - f_{LV} = r(1 - f_{LV})\cos \theta - f_{LV} = r\cos \theta - rf_{LV}\cos \theta - f_{LV} \quad (3)$$

where  $\theta_{CB}$  is the apparent contact angle of a rough surface,  $r$  is the roughness factor defined as a ratio of the actual surface area to the projected area,  $f_{SL}$  is the total area of the solid surface under the droplet per unit projected area under the droplet with  $\theta$  as the contact angle on the surface of material 1 ( $\theta$  is Young's contact angle of an ideal smooth homogeneous surface), and  $f_{LV}$  is the total area of air under the droplet per unit projected area under the droplet. The Cassie–Baxter model is based on the presence of air pockets on the roughened surface which will prevent water from wetting the entire surface [60]. According to (3), the contact angle of a hydrophilic surface can also increase to become a hydrophobic state as  $f_{LV}$  increases and meets the specific requirement shown in (4) [29,63]:

$$f_{LV} \geq \frac{r\cos \theta}{r\cos \theta + 1} \text{ for } \theta < 90^\circ \quad (4)$$

Chemical compositions on a surface determine the surface free energy (SFE) and by lowering the SFE, hydrophobicity is achieved [29]. The storage period of the samples in ambient conditions plays an important in changing the surface chemistry of the laser-structured regions. After two months under ambient conditions, the hydrophobic carbonaceous materials (e.g.,  $-\text{CH}_3$ ) were adsorbed on the laser-irradiated surfaces [9,50,53]. These carbonaceous materials are known to facilitate the achievement of hydrophobicity by the laser-irradiated surfaces over a period of time [5,17,61].

After the immersion of the laser-structured sample in seawater, the wetting behaviour of all regions changed from being a hydrophobic to a hydrophilic state, as shown in column red (CA 2) in Figure 8. This could be explained by a chemical state at the surface of the processed regions, where some Ti oxides (e.g.,  $\text{Ti}_2\text{O}_3$ ) present are known to have higher polarity and hence hydrophilic [5,33]. The photo-responsive nature of titanium oxide creates highly unstable oxygen vacancies which attract water and provide the functional  $-\text{OH}$  polar groups [66] which are known to have strong wettability [51,60]. The carbonaceous elements, which are hydrophobic, that had adsorbed on the surfaces initially (Table 3) might have desorbed, leaving the material to be hydrophilic. This can be confirmed from Table 3, where the C element is zero immediately after immersion.

The roughness of the surface structures could have played a role where wettability is enhanced by roughness as modelled by the Wenzel equation as given by (5) [67]:

$$\cos \theta_W = r \frac{\gamma_{SV} - \gamma_{SL}}{\gamma_{LV}} = r\cos \theta \quad (5)$$

where  $\theta_W$  is the apparent contact angle of a rough homogeneous surface,  $r$  is the roughness factor ( $r \geq 1$ , where  $r = 1$  for a perfectly planar surface and  $r > 1$  for a rough surface),  $\gamma_{SV}$ ,  $\gamma_{SL}$ , and  $\gamma_{LV}$  are the solid—vapour, solid—liquid, and liquid—vapour interfacial tensions, respectively [67,68]. The Wenzel equation (since  $r > 1$  as shown in (5)) shows that the hydrophilic surfaces become more hydrophilic when roughness increases [29]. It is assumed that water penetrated the valleys/grooves of the rough surface and completely wetted it. It was also noted during measurement after immersion that the wetting behaviour was a little anisotropic, and this shows that wettability was dependent on the morphological directions or surface chemistry.

After immersion, the sample was stored in ambient conditions for ten days. Then, contact angle measurements were performed again. It was noted that CAs were increasing again in some regions and transitioning to hydrophobic as shown in column blue (CA 3) in Figure 8. As explained, the transition is due to changes in the surface chemistry as a result of the adsorption of the non-polar carbon material on the surfaces of the laser-structured regions and the roughness of the laser-structured surfaces as per the modified Cassie–Baxter model.

Laser surface structuring alters the chemical composition, surface structure, and surface free energy (SFE) of the surface of a material. The SFE of the polished surface and the laser-structured surfaces of the CP Ti were determined by utilizing the Li–Neumann equation after measuring the contact angles of distilled water. The SFE of the polished CP Ti surface was  $44.08 \text{ mJ/m}^2$ . The values of the laser-structured surfaces obtained were plotted as shown in Figure S3 (Supplementary Information). From Figure S3, it can be noted that the SFE of the laser-structured surfaces before immersion was the lowest. Reduction of the SFE led to an increase in contact angles of the laser-structured surfaces of the CP Ti. The SFE of different regions of the laser-structured sample immediately after immersion is highest as seen from Figure S3. This increase is responsible for the highly hydrophilic behaviour of the laser-structured surfaces. The SFE at the surfaces determined ten days after immersion shows that the SFE is reducing, and the hydrophobicity is increasing. By considering the A1, B1, C1, D1, and E1 regions processed by different laser fluence but the same scanning velocity, hatching distance, and number of scanning passes, it can be noted from Figure S3 that, as the laser fluences increase, the values of the SFE reduces. By considering the A1, A2, A3, and A4 regions processed by the same laser fluence but different scanning velocities, hatching distance, and the number of scanning passes, it can be noted from Figure S3 that, as the scanning velocity and/or hatching distance increases, the values of the SFE increases. It is also noted that the plotted graph of the SFE is opposite to that of the plotted graph of the CA measurements. As the SFE increases, the CA reduces, and the opposite is true [28].

From the observations made, it can be stated that surface wettability is related to the changes to the surface chemistry and surface topography after laser structuring. The presence of rough surfaces after laser structuring enhances the hydrophobicity and the presence of hydrophobic carbon materials amplifies the attainment of the hydrophobicity. The changes in the transition of wettability show that laser structuring can be a promising tool to modify CP Ti surfaces to obtain desirable properties.

#### 4. Conclusions

In summary, this study reported on the study of the laser structuring of CP Ti surfaces using a picosecond laser with various laser processing parameters to fabricate surfaces with different surface morphologies, optical properties, surface chemistry, and wettability behaviours. After laser structuring, it was noted that a laser fluence of  $0.2 \text{ J/cm}^2$  generates HSFLs which are perpendicular to laser polarization and with periods in a range from 439 nm to 476 nm. The other laser fluences generate NC-LIPSS which are perpendicular to laser polarization and with periods in a range from 722 nm to 764 nm on the surface of the CP Ti material. The NC-LIPSS were decorated with nanodroplets. The morphologies at the ablated regions showed no signs of molten materials within its vicinity, hence the process at this low fluence can be described as a gentle ablation process. The EDX analysis reveals that the laser-structured surfaces had thin oxide films which increase as the laser fluences increase. The Raman analysis established that the thin oxide films formed on the surfaces of the laser-processed samples had a rutile-like phase of  $\text{TiO}_2$ , as shown by the established peaks, while the polished sample had no notable peaks. As the laser fluences increase, the intensity of the  $E_g$  and  $A_{1g}$  vibrational modes increases too.

The optical examinations show that different structural colours were produced in different regions. These colours have been attributed to the existence of various LIPSS generated on the laser-processed surfaces and/or titanium oxides present on the surfaces

of the laser-processed regions. Different LIPSS with various periods can produce different structural colours. It can also be stated that, after laser processing of CP Ti, the wettability of the substrate changes from a hydrophilic to a hydrophobic state. It was observed that the laser fluence increases with the CA and vice versa while for the hatching distance and/or scanning velocity, the CA reduces as the hatching distance increases. The SFE reduces as the laser fluence increases and vice versa. After immersion in seawater, the wetting behaviour changes to hydrophilic. After storage in ambient conditions, the sample transitioned again to a hydrophobic state. The surface structures and carbonaceous materials present play a major role in the wetting transition behaviour and depend on the storage conditions and time.

With this study, we have further enhanced the possibility of modifying the surface morphology, surface chemistry, optical properties, and wetting behaviour of CP Ti material directly through ultrafast laser surface structuring for different and tailored industrial applications such as wettability applications, anti-fouling control, corrosion control, decorations, photovoltaic cells, etc. In future work, optimizing and controlling the laser structuring of the surface towards a specific application can be considered. Further studies would be recommended to fabricate and evaluate the durability of the superhydrophobic surfaces on CP Ti substrate in real environments. Another piece of future work is to carry out more research to establish the contributions quantitatively of LIPSS, oxide films, and nanostructures to the colourization of metal surfaces after laser structuring.

**Supplementary Materials:** The following supporting information can be downloaded at: <https://www.mdpi.com/article/10.3390/app14083164/s1>. Figure S1: SEM micrographs of ps laser-structured CP Ti surfaces of regions shown on each image. The laser processing parameters indicated in Table 1 were applied to these regions. Figure S2: SEM images showing LIPSS on the laser-processed CP Ti surfaces of regions shown on each image after immersion. These regions were processed as per the parameters shown in Table 1. Figure S3: Surface free energy for laser-structured surfaces (A1, A2, A3, ..., E3, and E4) of the CP Ti before immersion (SFE 1), immediately after immersion (SFE 2) and 10 days after immersion (SFE 3).

**Author Contributions:** Conceptualization, K.R. and D.S.; methodology, K.R. and J.N.; software, K.R.; formal analysis, K.R.; investigation, K.R.; resources, A.K. and L.M.; data curation, K.R.; writing—original draft preparation, K.R.; writing—review and editing, J.N., D.S., A.K. and L.M.; visualization, K.R., A.K. and D.S.; supervision, D.S. and L.M.; funding acquisition, D.S. and L.M. All authors have read and agreed to the published version of the manuscript.

**Funding:** This research received no external funding.

**Institutional Review Board Statement:** Not applicable.

**Informed Consent Statement:** Not applicable.

**Data Availability Statement:** The original contributions presented in the study are included in the article/Supplementary Materials, further inquiries can be directed to the corresponding authors.

**Acknowledgments:** We acknowledge CzechNanoLab Research Infrastructure supported by MEYS CR (LM2023051). The research was supported by the Czech Academy of Sciences (RVO:68081731).

**Conflicts of Interest:** The authors declare no conflicts of interest.

## References

1. Ronoh, K.; Mwema, F.; Dabees, S.; Sobola, D. Advances in sustainable grinding of different types of the titanium biomaterials for medical applications: A review. *Biomed. Eng. Adv.* **2022**, *4*, 100047. [[CrossRef](#)]
2. Milovanović, D.; Rajčić, B.; Petronić, S.; Radulović, A.; Radak, B.; Gaković, B.; Zamfirescu, M.; Albu, C.; Savović, J. Comprehensive ablation study of near-IR femtosecond laser action on the titanium-based alloy Ti6Al4V: Morphological effects and surface structures at low and high fluences. *Eur. Phys. J. D* **2022**, *76*, 2. [[CrossRef](#)]
3. Haase, F.; Siemers, C.; Rösler, J. Laser powder bed fusion (LPBF) of commercially pure titanium and alloy development for the LPBF process. *Front. Bioeng. Biotechnol.* **2023**, *11*, 1260925. [[CrossRef](#)] [[PubMed](#)]

4. Fella, C.; Abida, B.; Samira, B.; El-Hadi, B.; Samia, A. Effects of Pulsed Laser Irradiation on Commercially Pure Titanium: Mechanical Properties and Corrosion Resistance in a Salty Environment. *Surf. Eng. Appl. Electrochem.* **2023**, *59*, 378–383. [[CrossRef](#)]
5. Exir, H.; Weck, A. Mechanism of superhydrophilic to superhydrophobic transition of femtosecond laser-induced periodic surface structures on titanium. *Surf. Coatings Technol.* **2019**, *378*, 124931. [[CrossRef](#)]
6. Ronoh, K.N.; Mwema, F.M.; Akinlabi, S.A.; Akinlabi, E.T.; Karuri, N.W.; Ngetha, H.T. Effects of cooling conditions and grinding depth on sustainable surface grinding of Ti-6Al-4V: Taguchi approach. *AIMS Mater. Sci.* **2019**, *6*, 697–712. [[CrossRef](#)]
7. Antończak, A.J.; Stępk, B.; Kozioł, P.E.; Abramski, K.M. The influence of process parameters on the laser-induced coloring of titanium. *Appl. Phys. A* **2014**, *115*, 1003–1013. [[CrossRef](#)]
8. Hulka, I.; Florido-Suarez, N.R.; Mirza-Rosca, J.C.; Saceleanu, A. Mechanical Properties and Corrosion Behavior of Thermally Treated Ti-6Al-7Nb Dental Alloy. *Materials* **2022**, *15*, 3813. [[CrossRef](#)] [[PubMed](#)]
9. Dou, H.-Q.; Liu, H.; Xu, S.; Chen, Y.; Miao, X.; Lü, H.; Jiang, X. Influence of laser fluences and scan speeds on the morphologies and wetting properties of titanium alloy. *Optik* **2020**, *224*, 165443. [[CrossRef](#)]
10. Yilbas, B.; Ali, H.; Al-Sharafi, A.; Al-Qahtani, H. Laser processing of Ti6Al4V alloy: Wetting state of surface and environmental dust effects. *Helijon* **2019**, *5*, e01211. [[CrossRef](#)]
11. Weng, W.-X.; Deng, Q.-W.; Yang, P.-Y.; Yin, K. Femtosecond laser-chemical hybrid processing for achieving substrate-independent superhydrophobic surfaces. *J. Central South Univ.* **2024**, *31*, 1–10. [[CrossRef](#)]
12. Kuczyńska-Zemka, D.; Sotniczuk, A.; Pisarek, M.; Chlenda, A.; Garbacz, H. Corrosion behavior of titanium modified by direct laser interference lithography. *Surf. Coatings Technol.* **2021**, *418*, 127219. [[CrossRef](#)]
13. Wang, Y.; Chen, J.; Yang, Y.; Liu, Z.; Wang, H.; He, Z. Nanostructured Superhydrophobic Titanium-Based Materials: A Novel Preparation Pathway to Attain Superhydrophobicity on TC4 Alloy. *Nanomaterials* **2022**, *12*, 2086. [[CrossRef](#)] [[PubMed](#)]
14. Kümmel, D.; Linsler, D.; Schneider, R.; Schneider, J. Surface engineering of a titanium alloy for tribological applications by nanosecond-pulsed laser. *Tribol. Int.* **2020**, *150*, 106376. [[CrossRef](#)]
15. Lian, Z.; Xu, J.; Yu, Z.; Yu, P.; Ren, W.; Wang, Z.; Yu, H. Bioinspired Reversible Switch between Underwater Superoleophobicity/Superaerophobicity and Oleophilicity/Aerophilicity and Improved Antireflective Property on the Nanosecond Laser-Ablated Superhydrophobic Titanium Surfaces. *ACS Appl. Mater. Interfaces* **2020**, *12*, 6573–6580. [[CrossRef](#)]
16. Simões, I.G.; dos Reis, A.C.; Valente, M.L.d.C. Influence of surface treatment by laser irradiation on bacterial adhesion on surfaces of titanium implants and their alloys: Systematic review. *Saudi Dent. J.* **2023**, *35*, 111–124. [[CrossRef](#)] [[PubMed](#)]
17. Vanithakumari, S.C.; Kumar, C.A.; Thinaharan, C.; Kishor, G.R.; George, R.P.; Kaul, R.; Bindra, K.S.; Philip, J. Laser patterned titanium surfaces with superior antifouling, superhydrophobicity, self-cleaning and durability: Role of line spacing. *Surf. Coatings Technol.* **2021**, *418*, 127257. [[CrossRef](#)]
18. Ahmed, K.M.T.; Grambow, C.; Kietzig, A.-M. Fabrication of Micro/Nano Structures on Metals by Femtosecond Laser Micromachining. *Micromachines* **2014**, *5*, 1219–1253. [[CrossRef](#)]
19. Yu, Z.; Yin, S.; Zhang, W.; Jiang, X.; Hu, J. Picosecond laser texturing on titanium alloy for biomedical implants in cell proliferation and vascularization. *J. Biomed. Mater. Res. Part B Appl. Biomater.* **2020**, *108*, 1494–1504. [[CrossRef](#)]
20. Li, Y.; Qian, J.; Bai, F.; Wang, Z.; Wang, C.; Fan, W.; Zhang, Y.; Zhao, Q. Azimuthal angle- and scanning pitch-dependent colorization of metals by ultrashort laser pulses. *Appl. Phys. A* **2016**, *122*, 282. [[CrossRef](#)]
21. Li, G.; Li, J.; Hu, Y.; Zhang, C.; Li, X.; Chu, J.; Huang, W. Femtosecond laser color marking stainless steel surface with different wavelengths. *Appl. Phys. A* **2015**, *118*, 1189–1196. [[CrossRef](#)]
22. Zhu, H.; Ehrhardt, M.; Lorenz, P.; Zajadacz, J.; Lu, J.; Zimmer, K. Combined effects of nanosecond laser-induced surface oxidation and nanostructure formation for selective colorization of nickel surfaces. *Appl. Phys. A* **2019**, *125*, 701. [[CrossRef](#)]
23. Vorobyev, A.Y.; Guo, C. Multifunctional surfaces produced by femtosecond laser pulses. *J. Appl. Phys.* **2015**, *117*, 033103. [[CrossRef](#)]
24. Vorobyev, A.Y.; Guo, C. Direct femtosecond laser surface nano/microstructuring and its applications. *Laser Photonics Rev.* **2013**, *7*, 385–407. [[CrossRef](#)]
25. Hermens, U.; Kirner, S.; Emonts, C.; Comanns, P.; Skoulas, E.; Mimidis, A.; Mescheder, H.; Winands, K.; Krüger, J.; Stratakis, E.; et al. Mimicking lizard-like surface structures upon ultrashort laser pulse irradiation of inorganic materials. *Appl. Surf. Sci.* **2017**, *418*, 499–507. [[CrossRef](#)]
26. Dusser, B.; Sagan, Z.; Soder, H.; Faure, N.; Colombier, J.; Jourlin, M.; Audouard, E. Controlled nanostructures formation by ultra fast laser pulses for color marking. *Opt. Express* **2010**, *18*, 2913–2924. [[CrossRef](#)] [[PubMed](#)]
27. Barmina, E.V.; Stratakis, E.; Fotakis, K.; Shafeev, G.A. Generation of nanostructures on metals by laser ablation in liquids: New results. *Quantum Electron.* **2010**, *40*, 1012–1020. [[CrossRef](#)]
28. Ronoh, K.; Novotný, J.; Mrňa, L.; Knápek, A.; Sobola, D. Effects of laser and scanning parameters on surface modification of MONEL®alloy 400 by picosecond laser. *Opt. Laser Technol.* **2024**, *172*, 110514. [[CrossRef](#)]
29. Mohamed, A.M.A.; Abdullah, A.M.; Younan, N.A. Corrosion behavior of superhydrophobic surfaces: A review. *Arab. J. Chem.* **2015**, *8*, 749–765. [[CrossRef](#)]
30. Rao, Q.; Weng, L.; Zhang, J.; Liu, D.; Zhang, W.; Chen, S.; Chen, J.; Li, X.; Qiu, H.; Cao, Y.; et al. Research Progress in Superhydrophobic Titanium-Based Implants for Antibacterial Applications. *Coatings* **2023**, *13*, 419. [[CrossRef](#)]

31. Ronoh, K.; Sobola, D.; Mrňa, L.; Novotný, J.; Dallaev, R.; Knápek, A.; Kolařík, V.; Holcman, V. Characterization of the picosecond laser-ablated HOPG using Raman spectroscopy and SEM microscopy. *Mater. Today Commun.* **2023**, *34*, 105181. [[CrossRef](#)]
32. Ronoh, K.N.; Novotný, J.; Mrňa, L.; Knápek, A.; Sobola, D. Analysis of processing efficiency, surface, and bulk chemistry, and nanomechanical properties of the Monel® alloy 400 after ultrashort pulsed laser ablation. *Mater. Res. Express* **2024**, *11*, 016514. [[CrossRef](#)]
33. Cunha, A.; Serro, A.P.; Oliveira, V.; Almeida, A.; Vilar, R.; Durrieu, M.-C. Wetting behaviour of femtosecond laser textured Ti–6Al–4V surfaces. *Appl. Surf. Sci.* **2013**, *265*, 688–696. [[CrossRef](#)]
34. Arasteh-Khoshbin, O.; Seyedpour, S.M.; Ricken, T. The effect of Caspian Sea water on mechanical properties and durability of concrete containing rice husk ash, nano SiO<sub>2</sub>, and nano Al<sub>2</sub>O<sub>3</sub>. *Sci. Rep.* **2022**, *12*, 20202. [[CrossRef](#)] [[PubMed](#)]
35. Tuzhilkin, V.S.; Katunin, D.N.; Nalbandov, Y.R. Natural Chemistry of Caspian Sea Waters. In *The Caspian Sea Environment*; Springer: Berlin/Heidelberg, Germany, 2005; pp. 83–108. [[CrossRef](#)]
36. Li, D.; Neumann, A. Equation of state for interfacial tensions of solid-liquid systems. *Adv. Colloid Interface Sci.* **1992**, *39*, 299–345. [[CrossRef](#)]
37. Ahadian, S.; Mohseni, M.; Moradian, S. Ranking proposed models for attaining surface free energy of powders using contact angle measurements. *Int. J. Adhes. Adhes.* **2009**, *29*, 458–469. [[CrossRef](#)]
38. Kalová, J.; Mareš, R. Reference Values of Surface Tension of Water. *Int. J. Thermophys.* **2015**, *36*, 1396–1404. [[CrossRef](#)]
39. Bonse, J.; Gräf, S. Maxwell Meets Marangoni—A Review of Theories on Laser-Induced Periodic Surface Structures. *Laser Photon. Rev.* **2020**, *14*, 2000215. [[CrossRef](#)]
40. Bonse, J.; Krüger, J.; Höhm, S.; Rosenfeld, A. Femtosecond laser-induced periodic surface structures. *J. Laser Appl.* **2012**, *24*, 042006. [[CrossRef](#)]
41. Vorobyev, A.Y.; Guo, C. Colorizing metals with femtosecond laser pulses. *Appl. Phys. Lett.* **2008**, *92*, 041914. [[CrossRef](#)]
42. Zhao, W.; Wang, W.; Jiang, G.; Li, B.Q.; Mei, X. Ablation and morphological evolution of micro-holes in stainless steel with picosecond laser pulses. *Int. J. Adv. Manuf. Technol.* **2015**, *80*, 1713–1720. [[CrossRef](#)]
43. Semaltianos, N.G.; Perrie, W.; French, P.; Sharp, M.; Dearden, G.; Logothetidis, S.; Watkins, K.G. Femtosecond laser ablation characteristics of nickel-based superalloy C263. *Appl. Phys. A* **2009**, *94*, 999–1009. [[CrossRef](#)]
44. Sharma, N.; Destouches, N.; Florian, C.; Serna, R.; Siegel, J. Tailoring metal-dielectric nanocomposite materials with ultrashort laser pulses for dichroic color control. *Nanoscale* **2019**, *11*, 18779–18789. [[CrossRef](#)] [[PubMed](#)]
45. Kobayashi, T.; Wakabayashi, T.; Takushima, Y.; Yan, J. Formation behavior of laser-induced periodic surface structures on stainless tool steel in various media. *Precis. Eng.* **2019**, *57*, 244–252. [[CrossRef](#)]
46. Segovia, P.; Wong, A.; Santillan, J.R.; Camacho-Lopez, M.; Camacho-Lopez, S. Multi-phase titanium oxide LIPSS formation under fs laser irradiation on titanium thin films in ambient air. *Opt. Mater. Express* **2021**, *11*, 2892–2906. [[CrossRef](#)]
47. Bizi-Bandoki, P.; Benayoun, S.; Valette, S.; Beaugiraud, B.; Audouard, E. Modifications of roughness and wettability properties of metals induced by femtosecond laser treatment. *Appl. Surf. Sci.* **2011**, *257*, 5213–5218. [[CrossRef](#)]
48. Ronoh, K.; Fawaeer, S.H.; Holcman, V.; Knápek, A.; Sobola, D. Comprehensive characterization of different metallic thin films on highly oriented pyrolytic graphite substrate. *Vacuum* **2023**, *215*, 112345. [[CrossRef](#)]
49. Florian, C.; Wonnerberger, R.; Undisz, A.; Kirner, S.V.; Wasmuth, K.; Spaltmann, D.; Krüger, J.; Bonse, J. Chemical effects during the formation of various types of femtosecond laser-generated surface structures on titanium alloy. *Appl. Phys. A* **2020**, *126*, 266. [[CrossRef](#)]
50. Yang, C.-J.; Mei, X.-S.; Tian, Y.-L.; Zhang, D.-W.; Li, Y.; Liu, X.-P. Modification of wettability property of titanium by laser texturing. *Int. J. Adv. Manuf. Technol.* **2016**, *87*, 1663–1670. [[CrossRef](#)]
51. Wang, Q.; Wang, H.; Zhu, Z.; Xiang, N.; Wang, Z.; Sun, G. Switchable wettability control of titanium via facile nanosecond laser-based surface texturing. *Surfaces Interfaces* **2021**, *24*, 101122. [[CrossRef](#)]
52. Conradi, M.; Kocijan, A.; Klobčar, D.; Godec, M. Influence of Laser Texturing on Microstructure, Surface and Corrosion Properties of Ti-6Al-4V. *Metals* **2020**, *10*, 1504. [[CrossRef](#)]
53. Dinh, T.-H.; Ngo, C.-V.; Chun, D.-M. Controlling the Wetting Properties of Superhydrophobic Titanium Surface Fabricated by UV Nanosecond-Pulsed Laser and Heat Treatment. *Nanomaterials* **2018**, *8*, 766. [[CrossRef](#)] [[PubMed](#)]
54. Hess, C. New advances in using Raman spectroscopy for the characterization of catalysts and catalytic reactions. *Chem. Soc. Rev.* **2021**, *50*, 3519–3564. [[CrossRef](#)] [[PubMed](#)]
55. Ekoi, E.; Gowen, A.; Dorrepaal, R.; Dowling, D. Characterisation of titanium oxide layers using Raman spectroscopy and optical profilometry: Influence of oxide properties. *Results Phys.* **2019**, *12*, 1574–1585. [[CrossRef](#)]
56. Wiatrowski, A.; Mazur, M.; Obstarczyk, A.; Wojcieszak, D.; Kaczmarek, D.; Morgiel, J.; Gibson, D. Comparison of the Physico-chemical Properties of TiO<sub>2</sub> Thin Films Obtained by Magnetron Sputtering with Continuous and Pulsed Gas Flow. *Coatings* **2018**, *8*, 412. [[CrossRef](#)]
57. Mino, L.; Mandrile, L.; Iannarelli, L.; Portesi, C.; Martra, G.; Rossi, A.M. Vibrational spectroscopy. In *Characterization of Nanoparticles*; Elsevier: Amsterdam, The Netherlands, 2020; pp. 457–480. [[CrossRef](#)]
58. Shaikh, S.; Kedia, S.; Majumdar, A.G.; Subramanian, M.; Sinha, S. In vitro bioactivity and biocompatibility of femtosecond laser-modified Ti<sub>6</sub>Al<sub>4</sub>V alloy. *Appl. Phys. A* **2018**, *124*, 821. [[CrossRef](#)]
59. Kristensen, A.; Yang, J.K.W.; Bozhevolnyi, S.I.; Link, S.; Nordlander, P.; Halas, N.J.; Mortensen, N.A. Plasmonic colour generation. *Nat. Rev. Mater.* **2016**, *2*, 16088. [[CrossRef](#)]

60. Riveiro, A.; Pou, P.; del Val, J.; Comesaña, R.; Arias-González, F.; Lusquiños, F.; Boutinguiza, M.; Quintero, F.; Badaoui, A.; Pou, J. Laser texturing to control the wettability of materials. In *Procedia CIRP*; Elsevier B.V.: Amsterdam, The Netherlands, 2020; pp. 879–884. [[CrossRef](#)]
61. Kietzig, A.-M.; Hatzikiriakos, S.G.; Englezos, P. Patterned Superhydrophobic Metallic Surfaces. *Langmuir* **2009**, *25*, 4821–4827. [[CrossRef](#)] [[PubMed](#)]
62. Cassie, A.B.D.; Baxter, S. Wettability of porous surfaces. *Trans. Faraday Soc.* **1944**, *40*, 546–551. [[CrossRef](#)]
63. Jung, Y.C.; Bhushan, B. Contact angle, adhesion and friction properties of micro-and nanopatterned polymers for superhydrophobicity. *Nanotechnology* **2006**, *17*, 4970–4980. [[CrossRef](#)]
64. Yan, Y.; Gao, N.; Barthlott, W. Mimicking natural superhydrophobic surfaces and grasping the wetting process: A review on recent progress in preparing superhydrophobic surfaces. *Adv. Colloid Interface Sci.* **2011**, *169*, 80–105. [[CrossRef](#)] [[PubMed](#)]
65. Boinovich, L.B.; Emelyanenko, A.M. Hydrophobic materials and coatings: Principles of design, properties and applications. *Russ. Chem. Rev.* **2008**, *77*, 583–600. [[CrossRef](#)]
66. Li, B.-J.; Li, H.; Huang, L.-J.; Ren, N.-F.; Kong, X. Femtosecond pulsed laser textured titanium surfaces with stable superhydrophilicity and superhydrophobicity. *Appl. Surf. Sci.* **2016**, *389*, 585–593. [[CrossRef](#)]
67. Wenzel, R.N. Resistance of solid surfaces to wetting by water. *Ind. Eng. Chem.* **1936**, *28*, 988–994. [[CrossRef](#)]
68. Manoharan, K.; Bhattacharya, S. Superhydrophobic surfaces review: Functional application, fabrication techniques and limitations. *J. Micromanufact.* **2019**, *2*, 59–78. [[CrossRef](#)]

**Disclaimer/Publisher's Note:** The statements, opinions and data contained in all publications are solely those of the individual author(s) and contributor(s) and not of MDPI and/or the editor(s). MDPI and/or the editor(s) disclaim responsibility for any injury to people or property resulting from any ideas, methods, instructions or products referred to in the content.